Journal of Fluids and Structures (2000) **14,** 87–101
doi:10.1006/jfls.1999.0253, available online at http://www.idealibrary.com on IDEAL®

AN INTEGRATED NONLINEAR APPROACH FOR TURBOMACHINERY FORCED RESPONSE PREDICTION. PART I: FORMULATION

A.I. Sayma, M. Vahdati and M. Imregun

Mechanical Engineering Department, Imperial College of Science Technology and Medicine, Exhibition Road, London SW7 2BX, U.K.

(Received 28 April 1998 and in final form 5 August 1999)

This paper describes the formulation of an advanced numerical model for the simulation of high- and low-engine-order forced response for turbomachinery applications. The various forced response mechanisms are explained in some detail and a specification for an accurate prediction system is discussed with emphasis on both fluid and structural modelling aspects. The Favre-averaged Navier–Stokes equations are used to represent the unsteady flow in a nonlinear time-accurate fashion. Features such as turbulence modelling, boundary conditions, meshing strategies and numerical treatments are discussed in detail. The structural model is based on a linear modal model, though local nonlinearities due friction dampers can be accommodated using an iterative scheme. The fluid mesh is moved at each-time step according to the structural motion, so that changes in blade aerodynamic damping and flow unsteadiness can be accommodated. It is concluded that the model can be used for large simulations involving multi-bladerow whole-annulus calculations.

1. NATURE OF THE PROBLEM

The forced response of bladed disks, in both axial and radial flows, is a very common vibration problem during the development phase of new gas turbines. A primary mechanism of blade failure is high-cycle fatigue (HCF) caused by vibrations at levels exceeding material fatigue endurance limits. Preventing turbomachinery blade failures is a necessary goal for engine manufacturers and, to this end, it is essential to prevent excessive vibration in turbomachinery blading due to forced excitation. The current state-of-art design techniques for estimating the forced response of turbomachinery blading are deficient in terms of predicting blade response levels quantitatively.

From the outset, it is appropriate to distinguish between two types of forced response. The first type, or classical forced response, is due to the excitation forces generated by the rotation of the bladed system past a pressure field, the strength of which varies periodically with angular position around the turbine. Such flow variations are mainly caused by the stator blades which act as upstream obstructions, and the rotor blades experience their wakes as time-varying forces with a frequency, or periodicity, based on the rotational speed. The spatial distribution of the forcing function will primarily be determined by the number of upstream stator blades and by its aliases with respect to the rotor blades. A Fourier transform of this forcing function will reveal the harmonics that will excite the assembly modes. Typically, such harmonics will excite high nodal diameter modes as their actual order is related to the blade numbers in the rotor/stator row of interest. Although it is difficult to predict the corresponding rotor blade vibration levels accurately, turbomachinery designers rely on Campbell diagrams (or their variants) which indicate the

0889–9746/00/010087 + 15 $35.00/0

likelihood of encountering forced response resonances of the first type within the operating range. In principle, it is then possible to design the rotor wheels away from the primary resonances, subject to being able to predict the dynamical behaviour of the assembly to a required degree of accuracy.

The second type of forced response, far less studied in the open literature, is much more difficult to deal with as the controlling parameters and the exact excitation mechanisms are poorly understood. However, the unsteady aerodynamic forcing function is known to be composed of low-order harmonics as it is responsible for exciting low-order nodal diameter assembly modes, hence the term "low-engine-order" (LEO) forced response. The main characteristics of the LEO forced response can be summarized as follows.

(i) It occurs at high speed and temperature and is most severe in the HP turbine, though it tends to persist throughout the engine. As will be discussed later, it is believed to be due to some loss of symmetry in the flow features.

(ii) It excites low nodal diameter fundamental blade modes which exhibit higher vibration levels. Hence, the likelihood of blade failure becomes high.

(iii) A large degree of response variability is observed from engine to engine. The same is also true of the particular low-engine-order harmonic that produces the highest response in a given nominal engine.

(iv) On rig tests, many of the highest measured responses in the running range are observed to be due to LEO excitation. Such situations require expensive modifications in relatively late stages of the design cycle. As the controlling mechanism is poorly understood, the use of friction dampers to reduce the response levels is often the only route available to the designer.

Forced response problems are not confined to turbine stages only. Some fans also experience forced response problems due to the wakes created by the inlet guide vanes (IGVs) and similar upstream obstructions. The situation is very similar to blade-passing excitation but the aerodynamic forcing may become very complex when IGVs have variable angles (Sayma *et al.* 1999). As for turbines, fans also suffer from low-engine-order excitation which usually arises from inlet distortions. Cross-wind effects and the intake geometry can also be very significant factors.

A detailed overview of turbomachinery aeroelasticity methods, including forced response prediction techniques, is discussed by Marshall & Imregun (1996). A brief summary will also be given here. Early studies were based on classical forced response models for cascades of flat plates which used wake coefficients. These were usually scaled to some arbitrary constant so that representative response levels could be obtained (Whitehead 1970; Nagashima & Whitehead 1977). Such models are also capable of handling potential disturbances. Erdos & Alzner (1977) were among the first researchers to investigate transonic cascade and blade number effects. Linearized models (Hall & Clark 1991; Holmes & Chuang 1991) have also been used to predict forced response. These methods solve the linearized field equations (potential or Euler) to obtain the unsteady pressures acting on the blade due to the incoming disturbances. In any case, the state of the art is to solve the fully nonlinear Euler or Navier–Stokes equations for the blade-row of interest, and to simulate the disturbance (wake or potential) moving past at blade passing velocity. Hodson (1985) and Giles (1988a) used the inviscid Euler equations to predict wake–rotor interaction. Similar work is also reported by Fransson & Pandolfi (1986) and Gerolymos (1988). A full stator–rotor interaction model using Navier–Stokes equations was developed in 2-D by Giles (1990b), and in 3-D by Rai (1987b). Results from some of the models above are compared with experimental data in the paper by Manwaring & Wisler (1992). A study of varying the blade numbers is reported by Korakianitis (1988). The paper by Chiang & Kielb

(1992), which presents an industrial forced response prediction system, also reviews much of the research in this area.

2. SPECIFICATION FOR A FORCED RESPONSE SYSTEM

Previous forced response studies have almost exclusively dealt with classical blade-passing forced response. However, from the above description, it is clear that a forced response prediction capability should be able to deal with both high and low-engine-order excitation. In any case, a forced response prediction system should consist of four parts: (i) flow defect modelling including intake distortion and cross-wind, (ii) unsteady aerodynamic modelling for gust response and aerodynamic damping, (iii) representative structural modelling, including nonlinear friction damping behaviour, and (iv) aeroelastic solution for the response of flexible blades.

One of the most important parts of a forced response system is an accurate and efficient flow solver which should possess the following features: (a) the ability to model three-dimensional flows and effects such as end-wall, tip leakage, etc., as these can contribute significantly towards the three dimensionality of the flow; (b) the ability to model both up- and down-stream pressure waves and their interactions; (c) the ability to model viscous effects from wakes, as they can contribute significantly towards the unsteady component of the flow; and (d) the ability to allow accurate transfer of information from one grid to another when multiple grids are used.

Most existing models are based on calculating the unsteady forces from the upstream and downstream distortions, independently of the blade's motion. The contribution of the blade vibration to the unsteady forces is usually calculated separately. The (positive) aerodynamic damping from the blade displacement is added to the (negative) contribution from the unsteady forcing to obtain the overall blade response. The advantage of performing forced response calculations in a coupled manner is that both the forcing and vibration effects are allowed to interact with each other, in an integrated fashion. There is experimental evidence that the unsteadiness due to blade motion can be significant (Manwaring *et al.* 1996). The current study is one of the first attempts at this kind of prediction.

3. SOURCES OF UNSTEADINESS

It is now appropriate to outline the sources and nature of various unsteady phenomena that are present in rotor–stator interactions. In the main, there are two sources of unsteadiness due to the relative motion of the stator and rotor rows, as follows.

(i) *Wake/rotor interaction*: The stator wakes, which can be assumed to be approximately steady in the stator frame of reference, are unsteady in the rotor frame of reference since the rotor is moving through them. Although the generation of the stator wakes is a viscous phenomenon, their subsequent interaction with the rotor blades is primarily an inviscid process. Therefore, it may be possible to perform an unsteady inviscid computation for the rotor domain, with the wakes being specified as unsteady inflow conditions obtained from a previous viscous calculation. However, the preferred approach is to perform a single viscous calculation for both domains.

(ii) *Potential stator/rotor interaction*: The unsteadiness can be explained by considering the three components of the pressure in the region between the stator and rotor bladerows: (i) uniform and steady, (ii) nonuniform but steady in the rotor frame, and (iii) nonuniform but steady in the stator frame. With rotation, both the stator and rotor blades experience unsteady forces that are due to the nonuniform pressure components. Such an interaction is

purely inviscid and can be modelled via the Euler equations. However, there is a need to consider the rotor and stator domains together when the spacing between the stator and rotor rows is small since the definition of unsteady rotor inlet boundary conditions will be very difficult in such cases.

The above sources of unsteadiness occur at blade-passing frequencies and excite the high nodal diameter assembly modes. Equally critical are the low-engine-order harmonics which are produced by the general unsteadiness of the flow throughout the engine. Industrial experience suggests that any loss of symmetry might give rise to such harmonics which are responsible for low-engine-order forced response. The following parameters are thought to be the most significant ones: inherent nonuniform spacing of the stator blades (also known as throat width variation), flow exit angle variations, axial gap changes between the rotor and stator blades, density variation due to combustion effects, combinations of blade numbers through several stages, nonsymmetric flows and temperature distributions due to burner blockages.

4. GENERAL FLOW MODELLING CONSIDERATIONS

The nature of the flow in modern turbomachines is complicated due to the co-existence of subsonic, supersonic and transonic regions in addition to shock waves and shock–boundary layer interactions. The situation is further compounded by the presence of acoustic waves which may cause acoustic resonances. Although much of the design work is based on the steady-state flow features at some nominal speed, the understanding of the unsteady flow is perhaps more important because of aeroelasticity considerations. Flutter and forced response, both part-speed phenomena, remain serious problems for engine integrity. In any case, a realistic simulation of turbomachinery aeroelasticity requires a time-accurate viscous representation of the unsteady compressible flow, a route which is computationally very expensive.

In recent years, the rapid development of numerical methods for the solution of the flow equations and the availability of powerful computers led to various prediction systems (Dawes 1988; Arnone 1995). Although external flow applications are dominated by unstructured grids (Barth 1990, 1991; Peraire *et al.* 1992; Venkata 1995; Mavriplis 1995; Frink 1996), most turbomachinery methods still use structured grids (Dawes 1988; Rai 1987a; Rai *et al.* 1990; Arnone 1995). While unstructured grids provide flexibility for discretizing complex geometries, they have the drawback of requiring larger in-core memory and more CPU effort than their structured counterparts.

However, the requirement to include complex geometric features such as tip gaps, cooling holes, snubbered fan blades, nonsymmetric intake ducts, struts, etc., can only be met via unstructured grids. Due to grid generation difficulties and flow solver limitations, unstructured grids generally use tetrahedral elements, even for turbomachinery applications (Vahdati & Imregun 1996). Although such grids are relatively easy to generate and efficient for capturing the inviscid features of the flow, the situation becomes more complicated in boundary layers, where large aspect ratio cells are required for computational efficiency. The gradients normal to the walls are several orders of magnitude larger than those along the walls; thus, more grid points are required in the former direction than the latter.

Such considerations led to the development of hybrid grid models where hexahedral or prismatic cells can be used in the boundary layers and tetrahedral and prismatic cells can be used to fill the domain away from the walls. For turbomachinery blades, Sbardella *et al.* (1997) presented a method to generate hybrid semi-structured grids where the boundary layers are filled with hexahedral cells and the rest of the domain is filled with triangular

prisms. Such a route not only provides a very efficient spatial discretization over standard unstructured grids but it also provides, for a comparable number of points, a much better grid quality over its fully structured counterparts. The same discretization strategy will also be used here.

5. THE FLOW MODEL

The unsteady, compressible, Favre-averaged Navier–Stokes equations for a 3-D blade-row can be cast in terms of absolute velocity **u** but solved in a relative non-Newtonian reference frame rotating with the blade about the x_1-axis with angular velocity ω. This system of equations, written in an arbitrary Eulerian Lagrangian (ALE) conservative form for a control volume Ω with boundary Γ, takes the form

$$\frac{\mathrm{d}}{\mathrm{d}t}\int_{\Omega}\mathbf{U}\,\mathrm{d}\Omega+\oint_{\partial\Omega}\left(\mathbf{F}-\frac{1}{\mathrm{Re}}\,\mathbf{G}\right)\cdot\boldsymbol{n}\,\mathrm{d}\Gamma=\int_{\Omega}\mathbf{S}\mathrm{d}\Omega, \tag{1}$$

$\boldsymbol{n}$ represents the outward unit vector of the control volume boundary Γ. The viscous term **G** on the left-hand side of equation (1) has been scaled by the reference Reynolds number for nondimensionalization purposes. The solution vector of conservative variables **U** is given by

$$\mathbf{U}=\begin{bmatrix}\rho\\ \rho\mathbf{u}\\ \rho e\end{bmatrix}. \tag{2}$$

The inviscid flux vector **F** has the following components:

$$\mathbf{F}=\mathbf{U}\mathbf{v}+\begin{bmatrix}0\\ p\delta_{ij}\\ u_j p\end{bmatrix}, \tag{3}$$

where δ_{ij} represents the Kronecker delta function and **v** is the velocity in the relative frame of reference. The pressure p and the total enthalpy h are related to density ρ, absolute velocity **u** and internal energy e by two perfect gas equations:

$$p=(\gamma-1)\rho\left[e-\frac{|\mathbf{u}|^2}{2}\right],\quad h=e+\frac{p}{\rho}, \tag{4}$$

where γ is the constant specific heat ratio. The viscous flux vector **G** has the following components:

$$\mathbf{G}=\begin{bmatrix}0\\ \sigma_{ij}\\ u_k\sigma_{ik}+\dfrac{\gamma}{\gamma-1}\left(\dfrac{\mu_l}{Pr_l}+\dfrac{\mu_t}{Pr_t}\right)\dfrac{\partial T}{\partial x_i}\end{bmatrix}. \tag{5}$$

The viscous stress tensor σ_{ij} is expressed using the eddy viscosity concept which assumes that, in analogy with viscous stresses in laminar flows, the turbulent stresses are proportional to the mean velocity gradients:

$$\sigma_{ij}=\mu\left(\frac{\partial u_i}{\partial x_j}+\frac{\partial u_j}{\partial x_i}\right)+\lambda\,\delta_{ij}(\nabla\cdot\mathbf{u}), \tag{6}$$

μ_l represents the molecular viscosity given by the Sutherland's formula, μ_t denotes the turbulent eddy viscosity, which must be determined by a suitable turbulence model. Therefore, $\mu = \mu_l + \mu_t$ is the total viscosity of the fluid. The value of λ is given by the Stokes relation $\lambda = -\frac{2}{3}\mu$ while the laminar Prandtl number, Pr_l, is taken as 0·7 for air. The turbulent Prandtl number, Pr_t, is taken as 0·9.

The term **S** in equation (1) is given by

$$\mathbf{S} = [0 \;\; 0 \;\; \rho\omega u_2 \;\; \rho\omega u_3 \;\; 0]^{\mathrm{T}}. \tag{7}$$

The eddy viscosity μ_t is calculated using the one-equation turbulence model of Baldwin & Barth (1991), though other one and two-equation turbulence models are also available in the aeroelasticity code used for this work.

6. NUMERICAL METHODOLOGY

The three-dimensional spatial domain is discretized using unstructured grids which, in principle, can contain cells with any number of boundary faces. The solution vector is stored at the vertices of the cells.

The present work uses semi-structured grids for their computational efficiency, although the solver is written for general hybrid unstructured grids. To achieve further computational efficiency, the mesh is represented using an edge base data structure. In this approach, the grid is presented to the solver as a set of node pairs connected by edges. The edge weights representing the inter-cell boundaries are computed in a separate pre-processor stage. Consequently, the solver has a unified data structure for which the nature of the hybrid mesh is concealed from the main calculation loops.

The flow model will now be explained in more detail. For clarity, the numerical discretization of the flow equations will be illustrated on a 2-D mesh. However, the resulting formulation is equally applicable to 3-D cells. Using an edge-based scheme, the typical 2-D mesh of Figure 1 can be discretized by connecting the median dual of the cells surrounding an internal node. For internal node I, the semi-discrete form can be written as

$$\frac{\mathrm{d}(\Omega_I \mathbf{U}_I)}{\mathrm{d}t} + \sum_{s=1}^{n_s} \frac{1}{2} \, |\boldsymbol{\eta}_{IJ_s}|(\mathscr{F}_{IJ_s} - \mathscr{G}_{IJ_s}) + B_i = \Omega_I \mathbf{S}_I, \tag{8}$$

where $\boldsymbol{\Omega}_I$ is the area of the control volume (shaded area in Figure 1), $\mathbf{U}_I$ is the solution vector at node I, n_s is the number of sides connected to node I, $\mathscr{F}_{IJ_s}$ and $\mathscr{G}_{IJ_s}$ are the numerical inviscid and viscous fluxes along side IJ_s, and B_i is the boundary integral. The side weight $\boldsymbol{\eta}_{IJ_s}$ is given by the summation of the two dual median lengths around the side times their normals. For example, the weight of the side connecting nodes I and J_1 is given by

$$\boldsymbol{\eta}_{IJ_1} = -\boldsymbol{\eta}_{J_1 I} = \vec{AB} + \vec{BC}. \tag{9}$$

In 3-D discretization, the resulting weights are the summation of the areas times their normal over the cell faces resulting from connecting the centroids of the cells and the middle points of the sides. The four-sided areas, resulting in hexahedral and prismatic cells, are calculated by dividing them into triangular faces in a consistent manner for the neighbouring cells such that the conservation property is assured. The resulting numerical scheme is second-order-accurate in space for tetrahedral meshes. For prismatic and hexahedral cells, the scheme is still second-order-accurate for regular cells with right angles. In the worst case of a highly skewed cell, the scheme will reduce to first-order accuracy (Essers *et al.* 1995). However, hexahedral meshes are usually generated in boundary layer where the generation

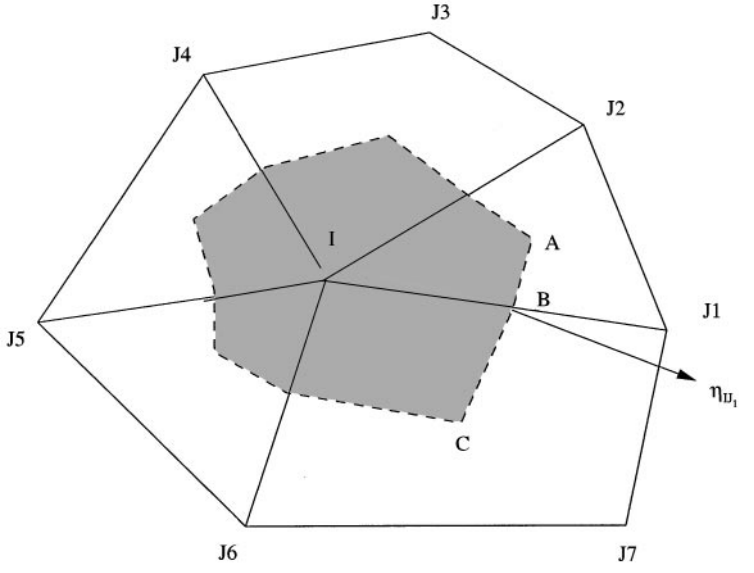

Figure 1. Typical 2-D mixed-cell mesh.

of regular cells to ensure orthogonality is relatively straightforward. Similarly, prismatic cells are usually generated in a structured manner by projecting triangular meshes on radial layers and then connecting them. Highly skewed meshes are unlikely to occur in such situations.

6.1 Inviscid Fluxes

The inviscid fluxes in equation (8) are expressed using a central difference formulation with a suitable artificial dissipation which is required to stabilize the scheme. Thus, inviscid fluxes can be written as

$$\mathscr{F}_{IJ_s} = \frac{\boldsymbol{\eta}_{IJ_s}}{|\boldsymbol{\eta}_{IJ_s}|} \cdot (\mathbf{F}_I + \mathbf{F}_{Js}) - \mathscr{D}_{IJ_s} \tag{10}$$

where $\mathscr{D}_{IJ_s}$ is the artificial dissipation along the side IJ_s. The artificial dissipation is based on an upwind scheme developed by Swanson & Turkel (1992), and Jorgenson & Turkel (1993). The scheme consists of a mixture of second- and fourth-order artificial viscosity. The fourth-order terms ensure the stability of the scheme in smooth flow regions The second-order terms are required to damp numerical oscillations in the vicinity of discontinuities where the scheme reverts to first order using a pressure-based sensor. The artificial dissipation can be written as:

$$\mathscr{D}_{IJ_s} = |A_{IJ_s}|[\phi(\mathbf{U}_{Js} - \mathbf{U}_I) - \varepsilon_4(1-\phi)(\mathscr{L}_{Js} - \mathscr{L}_I)], \tag{11}$$

where A_{IJ_s} is the standard Roe matrix (Roe 1981), $\varepsilon_4 \approx \frac{1}{8}$ is the fourth-order artificial dissipation coefficient and $\mathscr{L}$ is a pseudo-Laplacian operator,

$$\mathscr{L}\left(\mathbf{U}_I\right) = \left(\sum_{s=1}^{n_s} \frac{\mathbf{U}_{Js} - \mathbf{U}_I}{S_{IJ_s}}\right)\left(\sum_{s=1}^{n_s} \frac{1}{S_{IJ_s}}\right)^{-1}, \tag{12}$$

where $S_{IJ_s} = |\mathbf{x}_{Js} - \mathbf{x}_J|$. Moreover, ϕ is the second-order flux limiter which is required to enforce the monotonicity of the scheme given by

$$\phi = \max(\phi_I, \phi_{Js}), \tag{13}$$

where

$$\phi_I = \frac{2|p_{Js} - p_I - \boldsymbol{S}_{IJ_s}(\boldsymbol{\nabla}p)_{Js}|}{(1-\omega)[|p_{Js} - p_I| + |p_I - p_{Js} + 2(\boldsymbol{\nabla}p)_{Js}\boldsymbol{S}_{IJ_s}|] + 2\omega[p_{Js} + p_I + \boldsymbol{S}_{IJs}(\boldsymbol{\nabla}p)]}, \tag{14}$$

with $\omega \approx 0{\cdot}5$; ϕ_{Js} can similarly be obtained from equation (14) by substituting Js for I.

6.2. Viscous Fluxes

The viscous fluxes are treated within the same edge-based data structure framework, provided the gradients of the primitive variables are known at the mesh nodes. Using the edge weights of equation (9), these gradients can be calculated from the formula

$$\left[\Omega \frac{\partial}{\partial\theta} x_j\right]_I = \sum_{s=1}^{n_s} \frac{1}{2} \eta_{IJ_s}(\theta_I + \theta_{Js}) + B_i, \tag{15}$$

where θ represents a generic primitive variable and B_i is the boundary integral arising from the contributions of the boundary faces at the domain boundaries. This formulation results in a viscous flux scheme which uses information from two layers of points surrounding the point under consideration. The choice of this scheme is purely for computational efficiency and storage economy. The use of a finite element approach will require the storage of nine additional quantities per side. In any case, numerical experiments show that there is a negligible difference between the two approaches.

6.3. Implicit Temporal Discretization

Equation (8) can be expressed in the form

$$\frac{\mathrm{d}(\Omega_I U_I)}{\mathrm{d}t} = \mathbf{R}(\mathbf{U}). \tag{16}$$

A second-order implicit backward time integration of equation (16) can be expressed as

$$\frac{3(\Omega\mathbf{U})_I^{n+1} - 4(\Omega\mathbf{U})_I^n + (\Omega\mathbf{U})_I^{n-1}}{2\Delta t} = \mathbf{R}(\mathbf{U}^{n+1}), \tag{17}$$

where n denotes the time level. The implicit nonlinear system of equations given by equation (17) needs to be solved at every time-step. An iterative equation is constructed from equation (17) by simply adding a pseudo-time derivative term $\mathbf{U}_\tau$ to the left-hand side,

$$\mathbf{U}_\tau + \frac{3(\Omega\mathbf{U})_I^{n+1} - 4(\Omega\mathbf{U})_I^n + (\Omega\mathbf{U})_I^{n-1}}{2\Delta t} = \mathbf{R}(\mathbf{U}^{n+1}). \tag{18}$$

Indicating with $\mathbf{U}^m$ the mth approximation to $\mathbf{U}^{n+1}$, equation (18) can be re-written as

$$\Omega_I^{n+1}\left(\frac{1}{\Delta\tau} + \frac{3}{2}\frac{1}{\Delta t}\right)\Delta\mathbf{U}_I + \frac{3\Omega_I^{n+1}\mathbf{U}_I^m - 4(\Omega\mathbf{U})_I^n + (\Omega\mathbf{U})_I^{n-1}}{2\Delta t} = \mathbf{R}^{m+1}, \tag{19}$$

where $\Delta\mathbf{U}_I = \mathbf{U}_I^{m+1} - \mathbf{U}_I^m$, $\Delta\tau$ representing the pseudo-time-step. Linearizing the right-hand side of equation (19) around $\mathbf{U}_I^m$, the pseudo-time integration which advances the

solution from t^n to t^{n+1} becomes

$$\left(\frac{\Omega_I^{n+1}}{\Delta\tau}+\frac{3}{2}\frac{\Omega_I^{n+1}}{\Delta t}-\mathbf{J}^m\right)\Delta\mathbf{U}_I=\mathbf{R}^m-\frac{3}{2}\frac{\Omega_I^{n+1}}{\Delta t}\mathbf{U}_I^m-\mathbf{E}_I^n, \tag{20}$$

where $\mathbf{E}_I^n$ involves the portion of the physical time derivative at previous time-steps and is invariant during the iteration process:

$$\mathbf{E}_I^n=\frac{4(\Omega\mathbf{U})_I^n-(\Omega\mathbf{U})_I^{n-1}}{2\Delta t}. \tag{21}$$

The left-hand side of equation (20) contains a portion of the physical-time derivative in order to reduce the pseudo-time-step in regions of the flow where the ratio pseudo/physical time-step, $\Delta\tau/\Delta t$, becomes large (Melson *et al*. 1993). Equation (20) is solved iteratively until the term $\Delta\mathbf{U}_I$ is driven to a specified small tolerance. Within this iteration level, a Jacobi sub-iteration procedure is performed to solve the linearized system of equations described by equation (20).

Time accuracy is guaranteed by the outer iteration level where the time-step is fixed throughout the solution domain, while the inner iteration procedure can be performed using traditional acceleration techniques such as local time-stepping and residual smoothing.

6.4. Boundary Conditions

This section describes the numerical treatment of the inflow and outflow boundaries for turbomachinery flow calculations. Whereas the far-field boundaries for isolated aerofoils can be taken many chords away, the boundaries are typically less than one chord away for most turbomachinery applications. This situation may lead to computational inaccuracies if the boundary conditions are not suitably formulated. Various techniques have been developed to minimize the reflection of the outgoing waves (Engquist & Majda 1977; Higdon 1986; Ferm 1995; Giles 1990a) and an overview is given by Givoli (1991). Here two different set of treatments, one for steady-state computation and the other for unsteady computation, are used. The steady-state boundary treatment is based on the characteristics of the Euler equations. In particular, the steady-state boundary conditions are obtained from the linear, harmonic unsteady nonreflecting boundary conditions, as a limiting case of zero-frequency unsteadiness. The resulting nonreflecting boundary conditions are exact for linear solutions at the far-field boundary. The treatment of such boundary conditions for 2-D turbomachinery applications can be found in Giles (1988b). An extension to 3-D is reported by Giles (1990a).

Two further types of boundary conditions are needed for turbomachinery calculations: solid wall and periodicity. On solid walls, the pressure is extrapolated from the interior points and the slip (inviscid) or no-slip (viscous) conditions are used to compute the other quantities. An extra boundary condition for the heat flux is employed for viscous flow calculations. Using the edge-based data structure, the periodicity is handled in a straightforward way as long as the points in the two periodic boundaries are located at same axial and radial coordinates.

6.5. Treatment of the Sliding Boundaries

From a computational point of view, one major difficulty in simulating rotor–stator flows arises because of the relative motion between the rotor and stator blades. One of the most

straightforward solutions to this problem is to use two grids that move relative to each other. Typically, one would use a stationary grid to discretize the stator blades and a moving grid (stationary with respect to the rotor) to represent the rotor blades. For a given rotation between the stator and the rotor blade-rows, the flow solution at the interface must be determined. In the procedure used here, the solution is updated at the interface in a conservative manner by linearly interpolating the variables in the stator computational domain to obtain rotor fluxes, and in the rotor computational domain to obtain the stator fluxes. The fluxes are computed by using a characteristic technique which allows the correct propagation of the information and the interface is updated at the end of each time-step. In other words, flow data are exchanged between the two grids via specially formulated boundary conditions at the interface. Numerical experience indicates that the current implementation, based on the formulation of Rai (1986) is numerically stable, spatially and temporally accurate, and conservative so the flow discontinuities can move from one grid to another without causing distortions.

7. STRUCTURAL MODEL

From the outset, it should be stressed that the dynamic behaviour of the bladed-disk structure is nonlinear since it includes a large number of friction dampers. Further, structural nonlinearities include snubbers, shroud interfaces and large amplitude motion. For a nonlinear structure, the most general approach would be the formulation and the direct time integration of the mass, stiffness and damping matrices, using the physical coordinates as the dependent variables. The aerodynamic load vector at each time-step would then be obtained by interpolating the fluid pressure onto the structural grid, the nodal forces being computed from the product of this pressure by the corresponding area. New positions and velocities of each structural node could be interpolated back onto the fluid grid, to obtain its new position and velocity for the next time-step. However, the calculation of the aeroelastic motion by this method would be computationally very expensive, and a formulation that can reduce the computational effort is highly desirable. For a linear structure, such an aim can easily be achieved by uncoupling the structural equations of motion by a coordinate transformation via the mode shape matrix[†]. For the linear part of the system, the reduced modal equations can be solved by time- marching, with the modal matrix providing the link between the principal coordinates in the equation of motion (EOM) and the physical coordinates of the structure. The mode shape vectors can then be interpolated onto the aerodynamic grid points at the start of the calculation. Although no further interpolation is required, the mesh is still moved at each time-step to accommodate the aeroelastic motion, a feature that will be discussed later. Assuming, for the time being, that the structure is linear, the aeroelastic EOM can be written as:

$$[\mathbf{M}]\{\ddot{\boldsymbol{x}}\} + [\mathbf{C}]\{\dot{\boldsymbol{x}}\} + [\mathbf{K}]\{\boldsymbol{x}\} = \{p(t)\boldsymbol{n}\}, \tag{22}$$

where **M**, **C**, **K** are the mass, structural damping and stiffness matrices, **x** is the mode shape vector, $p(t)$ is the pressure and $\boldsymbol{n}$ is the normal unit vector on the blade surface. The free vibration problem can be solved to yield natural frequencies, ω_i, and the mass-normalized mode shape matrix $[\boldsymbol{\Phi}]$. The centrifugal stiffening effects are taken into account by adding the appropriate terms to the stiffness matrix. Equation (22) is usually solved for a typical sector, which also includes the disk for turbine cases. The mode shapes of the full assembly are then obtained by expanding the cyclic symmetry mode shapes. Many such typical sector

[†] The nonlinear behaviour due to the presence of the friction dampers will be studied in a separate section.

analyses are performed to cover all assembly modes of interest. The required coordinate transformation is

$$\{\boldsymbol{x}\} = [\boldsymbol{\Phi}]\{\boldsymbol{q}\}, \tag{23}$$

where **q** is the vector of the principal or modal coordinates. Using equations (22) and (23) and pre-multiplying by $[\boldsymbol{\Phi}]^{\mathrm{T}}$:

$$[\boldsymbol{\Phi}]^{\mathrm{T}}[\boldsymbol{M}][\boldsymbol{\Phi}]\{\ddot{\boldsymbol{q}}\} + [\boldsymbol{\Phi}]^{\mathrm{T}}[\mathbf{C}][\boldsymbol{\Phi}]\{\dot{\boldsymbol{q}}\} + [\boldsymbol{\Phi}]^{\mathrm{T}}[\mathbf{K}][\boldsymbol{\Phi}]\{\boldsymbol{q}\} = [\boldsymbol{\Phi}]^{\mathrm{T}}\{p(t)\boldsymbol{n}\}. \tag{24}$$

The structural equations of motion can be reduced further by removing both the coordinates and modes that are of no interest in the flutter calculations. Assuming proportional damping (without loss of generality) and using the orthogonality properties of the system matrices with respect to the mode shape matrix, one obtains

$$\{\boldsymbol{q}\}_N + [\mathrm{diag}(2\zeta_i\omega_i)]_{N\times N}\{\dot{\boldsymbol{q}}\}_N + [\mathrm{diag}(\omega_i^2)]_{N\times N}\{\boldsymbol{q}\}_N = [\boldsymbol{\Phi}]^{\mathrm{T}}_{m\times N}\{\mathbf{p}(t)\}_m = [\boldsymbol{\Pi}(t)]_N, \tag{25}$$

where ω_i and ζ_i are the natural frequency and modal damping for mode i, N is the number of structural coordinates and m is the number of modes.

The right-hand-side vector of modal forces is formed as follows:

$$\boldsymbol{\Pi}(t) = [\boldsymbol{\Phi}]^{\mathrm{T}}\{P(t)\boldsymbol{n}\} = \left\{\left(\sum_{i=1}^{n_a} p_i\phi_{i,r}\right)\cdot\boldsymbol{n}_i\right\}_{r=1,m}, \tag{26}$$

where n_a is the number of aerodynamic nodes on the blade surface.

In this form, the equations of motion can be solved by any standard numerical integration scheme and the self-starting, second-order-accurate and unconditionally stable Newmark discretization (Newmark 1959) was used in the current work.

7.1. Mesh Movement

When undertaking a forced response aeroelasticity analysis, it is desirable to move the fluid mesh according to the instantaneous position of body under consideration so that the blade vibration can be included in the calculations. This requirement is met by using an algorithm which considers the mesh as a network of springs whose extension/compression is prescribed by the mode shape at the blade surface and becomes zero at the far field. At each node, the spring stiffnesses are allocated values that are inversely proportional to the length of the shared edge lengths. The CFD algorithm takes full account of the unsteady fluxes which arise due to cell volume changes at each time-step.

7.2. Friction Dampers

One way of minimizing the resonant response is to introduce additional damping. Very few solutions exist at high temperatures but friction or underplatform dampers provide a robust means of preventing the vibration levels from reaching high amplitudes. Friction dampers are small pieces of metal loaded on the underside of adjacent blade platforms by the centrifugal force. A most common type, the so-called cottage roof damper, is shown in Figure 2. The basic idea is to maximize the friction area for increased energy dissipation. The assumed elliptical path of the friction contact is shown in Figure 3. If the damper mass is too small, the friction force will not be large enough to dissipate sufficient energy. On the other hand, a large mass will limit the relative motion, again decreasing the damping properties. From such considerations, it is clear that, for a given geometry and relative motion, there will be an optimum size which will yield maximum energy dissipation. Due to

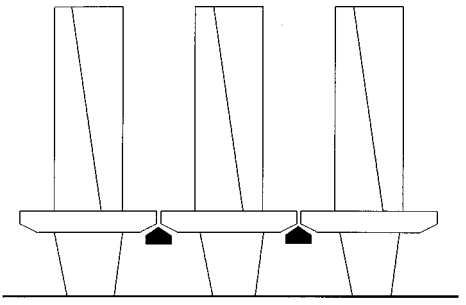

Figure 2. Under-platform cottage-roof dampers between adjacent blades [from Sanliturk *et al.* (1999)].

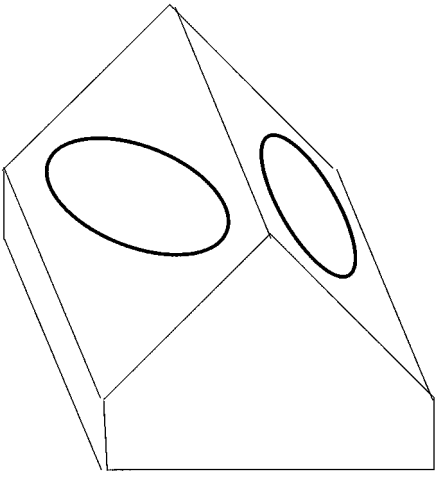

Figure 3. Assumed elliptical path of the friction contact [from Sanliturk *et al.* (1999)].

strong nonlinear behaviour, the theoretical analysis and the optimization of friction dampers is a difficult topic but major advances have been made in the last five years (Sanliturk & Ewins 1996, 1997; Sanliturk *et al.* 1999; Yang & Meng 1997).

Friction dampers are usually characterized by their force–displacement hysteresis loops, the determination of which is based on a mixture of analytical and experimental techniques. Under some simplifying assumptions, it is possible to derive expressions for the damper forces and use experimentally derived coefficients.

With the inclusion of the damper forces $\{\boldsymbol{f}_{FD}(\boldsymbol{x})\}$, equation (22) becomes

$$[\mathbf{M}]\{\ddot{\boldsymbol{x}}\} + [\mathbf{C}]\{\dot{\boldsymbol{x}}\} + [\mathbf{K}]\{\boldsymbol{x}\} = \{p(t)\mathbf{n}\} + \{\boldsymbol{f}_{FD}(\boldsymbol{x})\}. \tag{27}$$

A frequency domain solution of equation (27) is discussed in some detail in Sanliturk *et al.* (1997). In the time-domain scheme employed here, the friction damper forces are computed using the same formulation and they are added to the aerodynamic forces.

A major difficulty arises when performing forced response calculations with friction dampers, as such devices may change the resonant frequency by as much as 15%. A straightforward solution would be to sweep the speed range by performing separate calculations at each point. The problem is further compounded by the fact that aerodynamic

boundary conditions are rarely available at all speeds of interest. Given the impracticalities of using a nonlinear time-marching code in this fashion, some iterative procedure needs to be employed to track the resonance. Such a route was adopted here.

8. CONCLUDING REMARKS

The following concluding remarks may be made.

(i) An advanced numerical model for the forced response analysis of turbomachinery blades was presented. The model, which uses nonlinear representations for both the structure and the fluid, can deal with turbine and compressor-forced response arising from low- and high-engine-order harmonics.

(ii) The flow discretization is via unstructured hybrid grids and the solver has an edge-based data structure. Implicit dual time stepping is employed for time-accurate viscous unsteady flows.

(iii) The structural model is based on a linear modal model, though local non-linearities due friction dampers can be accommodated using an iterative scheme. Numerical experience indicates the time integration is impracticable with large mass, stiffness and damping matrices.

(iv) The generality of the numerical model will allow the direct simulation of blade mistuning. however, the objective of such investigation should be to relate statistical properties of blade mistuning to those of the ensuing response. A detailed study of a particular mistuning pattern is likely to be less useful, other than perhaps, for the validation of a perturbation-type analysis.

(v) The blade motion may change both the aerodynamic damping and the flow unsteadiness. The proposed approach is using moving meshes, such that such features are automatically included in the analysis.

(vi) The model is found to be computationally efficient and, as will be shown in the second part of the paper, it enables to undertake large unsteady viscous flow simulations with current computing power.

(vii) Parallelization on distributed memory machines is currently in progress and it is expected that whole-annulus multi-blade-row computations will become commonplace before the end of the century.

ACKNOWLEDGEMENTS

The authors would like to thank Rolls-Royce plc for both sponsoring this work and allowing its publication. They also thank their colleagues Dr K. Y. Sanliturk, Dr R. M. Hall, Mr R. Elliott and Mr J. S. Green for many useful discussions.

References

ARNONE, A. 1995 Multigrid methods for turbomachinery Navier–Stokes calculations. In *Solution Techniques for Large-Scale CFD Problems* (ed. W. Habashi), pp. xx–yy.

BALDWIN, B. S. & BARTH, T. J. 1991 A one-equation turbulence transport model for high Reynolds number wall-bounded flows. AIAA paper 91–0610.

BARTH, T. J. 1990 On unstructured grid solvers. Technical Report VKI-LS, Lecture Series 1990–03, Von Karman Institute Publications.

BARTH, T. J. 1991 Numerical aspects of computing high Reynolds number flows on unstructured meshes. AIAA Paper 91–0721.

CHIANG, H. D. & KEILB, R. E. 1992 An analysis system for blade forced response . ASME paper 92-GT-17.

DAWES, W. N. 1988 Development of a three-dimensional Navier–Stokes solver for application to all types of turbomachinery. ASME Paper 88-GT-70.
ENGQUIST, B. & MAJDA, A. 1977 Absorbing boundary conditions for the numerical simulation of waves. *Mathematics of Computation* **31,** 629–651.
ERDOS, J. I. & ALZNER 1977. Computation of unsteady transonic flows through rotating and stationary cascades. NASA CR - 2900.
ESSERS, J. A., DELANAYE, M. & ROGIEST, P. 1995 Upwind-biased finite-volume technique solving Navier–Stokes equations on irregular meshes. *AIAA Journal* **33,** 833–842.
FERM, L. 1995 Non-reflecting boundary conditions for the steady euler equations. *Journal of Computational Physics* **122,** 307–316.
FRANSSON, T. H. & PANDOLFI, M. 1986 Numerical investigation of unsteady subsonic compressible flows through an oscillating cascade . ASME Paper 86-GT-304.
FRINK, N. T. 1996 Assessment of an unstructured-grid method for predicting 3-D turbulent viscous flows. AIAA Paper 96-0292.
GEROLYMOS, G. A. 1988 Numerical integration of the blade-to-blade surface Euler equations in vibrating cascades. *AIAA Journal* **26,** 1483–1492.
GILES, M. B. 1988a Calculation of unsteady wake/rotor interaction. *AIAA Journal of Propulsion* **4,** 356–362.
GILES, M. B. 1988b Non-reflecting boundary conditions for the euler equations. Technical Report TR-88-1, Computational Fluid Dynamics Lab, MIT, Cambridge, MA, U.S.A.
GILES, M. B. 1990a Non-reflecting boundary conditions for the Euler equations calculations. *AIAA Journal* **28,** 2050–2058.
GILES, M. B. 1990b Stator/rotor interaction in a transonic turbine. *AIAA Journal of Propulsion and Power* **6,** 621–627.
GIVOLI, D. 1991 Non-reflecting boundary conditions. *Journal of Computational Physics* **94,** 1–29.
HIGDON, R. L. 1986 Absorbing boundary conditions for difference approximations to the multi-dimensional wave equation. *Mathematics of Computation* **47,** 437–459.
HODSON, H. P. 1985. An inviscid blade-to-blade prediction of a wake-generated unsteady flow. *ASME*: *Journal of Engineering for Gas Turbines and Power* **107,** 337–343.
HOLMES, D. G. & CHUANG, H. A. 1991. Two dimensional linearized harmonic Euler flow analysis for flutter and forced response. *In* 6th UAATP, Notre Dame, U.S.A.
JORGENSON, P. C. & TURKEL, E. 1993 Central difference TVD schemes for time dependent and steady state problems. *Journal of Computational Physics* **107,** 297–308.
KORAKIANITIS, N. M. 1988 On the prediction of unsteady forces on gas turbine blades—Parts 1 & 2. ASME Papers 88-GT-89 & 88-GT-90.
MANWARING, S. R. & WISLER, D. C. 1992 Unsteady aerodynamics and gust response in compressors and turbines. ASME Paper 92-GT-422.
MANWARING, S. R. RABE, D. C., LORENCE, C. B. & WADIA, A. R. 1996 Inlet distortion generated forced response of a low aspect ratio transonic fan. ASME Paper 96-GT-376.
MARSHALL, J. G. & IMREGUN, M. 1996. A review of aeroelasticity methods with emphasis on turbomachinery applications. *Journal of Fluids and Structures* **10,** 237–267.
MAVRIPLIS, D. J. 1995 Three-dimensional multigrid reynolds-averaged Navier–Stokes solver for unstructured meshes. *AIAA Journal* **3,** 445–453.
MELSON, N. D., SANETRIK, M. D. & ATKINS, H. L. 1993 Time-accurate Navier–Stokes calculations with multigrid acceleration. *Proceedings of the Sixth Copper Mountain Conference on Multigrid Methods.*
NAGASHIMA, T. & WHITEHEAD, D. S. 1977 Linearized supersonic unsteady flow in cascades. A.R.C. R & M. No. 3811.
NEWMARK, N. M. 1959 A method of computation for structural dynamics. *ASCE Journal of Engineering Mechanics Division* **8,** 67–94.
PERAIRE, J., MORGAN, K., VAHDATI, M. & PEIRÓ, J. 1992 The construction and behavior of some unstructured grid algorithms for compressible flows. In *ICFD Conference on Numerical Methods for Fluid Dynamics.* Oxford: Oxford University Press.
RAI, M. M. 1986 implicit conservative zonal boundary scheme for Euler equations calculations. *Computers and Fluids* **14,** 295–319.
RAI, M. M. 1987a Navier-Stokes simulations of rotor/stator interaction using patched and overlaid grids. *AIAA Journal of Propulsion and Power* **3,** 387–396.
RAI, M. M. 1987b. Unsteady 3D Navier–Stokes simulations of turbine rotor-stator interaction. AIAA Paper 87–2038.

RAI, M. M. & MADAVAN, N. K. 1990 Multi-airfoil Navier–Stokes simulations of turbine rotor-stator interaction. *ASME Journal of Turbomachinery* **112,** 377–384.

ROE, P. 1981 Approximate Riemann solvers, parameter vectors and difference schemes. *Journal of Computational Physics* **43,** 357–372.

SANLITURK, K. Y. & EWINS, D. J. 1996 Modelling two-dimensional friction contact and its application using harmonic balance method. *Journal of Sound and Vibration* **193,** 511–523.

SANLITURK, K. Y. & EWINS, D. J. 1997 Harmonic balance vibration analysis of turbine blades with friction dampers. *ASME Journal of Vibration and Acoustics* **119,** 96–103.

SANLITURK, K. Y., EWINS, D. J. & STANBRIDGE, A. B. 1999. Underplatform dampers: theoretical modelling, analysis and comparison with experimental data. 44*th ASME Gas Turbine and Aeroengine Technical Congress*, Indianapolis, IN, U.S.A.

SAYMA, A. I., VAHDATI, M. & IMREGUN, M. 1999. Fan forced response predictions due to inlet distortions and excitation from inlet guide vanes at high deflection. *Fourth National Turbine Engine High Cycle Fatigue Conference*, Monterey, CA, U.S.A.

SBARDELLA, L., SAYMA, A. I. & IMREGUN, M. 1997. Semi-unstructured mesh generator for flow calculations in axial turbomachinery blading. 18*th International Symposium on Unsteady Aerodynamics and Aeroelasticity of Turbomachines* (ed. T. Fransson), pp. xx–yy. Kluwer Academic Publishers.

SWANSON, R. C. & TURKEL, E. 1992. On central-difference and upwind Schemes. *Journal of Computational Physics* **101,** 292–306.

VAHDATI, M. & IMREGUN, M. 1996 Non-linear aeroelasticity analysis of a fan blade using unstructured dynamic meshes. *IMechE Journal of Mechanical Engineering Science* **210,** 549–564.

VENKATAKRISHNAN, V. 1995 A prospective on unstructured grid flow solvers. Technical Report 95-3, ICASE.

WHITEHEAD, D. S. 1970 Vibration and sound generation in a cascade of flat plates in subsonic flow. A.R.C. R & M. No. 3865.

YANG, B. D. & MENG, C. H. 1997 Characterisation of contact kinematics and application to the design of wedge dampers in turbomachinery blading—Parts I and 2. ASME Papers 97-GT-19 and 97-GT-20.